

# A numerical wave-optical approach for the simulation of analyzer-based x-ray imaging

A. Bravin<sup>1\*</sup>, V. Mocella<sup>2</sup>, P. Coan<sup>1</sup>, A. Astolfo<sup>1,3</sup>, and C. Ferrero<sup>1</sup>

<sup>1</sup>European Synchrotron Radiation Facility, BP220, 6 rue J. Horowitz, F-38043 Grenoble Cedex, France

<sup>2</sup>CNR - IMM - Sezione di Napoli, via P. Castellino 111, I-80131 Napoli, Italy

<sup>3</sup>Università degli Studi di Trieste, Dipartimento di Fisica, via Valerio 2, 34126 Trieste, Italy

\*bravin@esrf.fr

**Abstract:** An advanced wave-optical approach for simulating a monochromator-analyzer set-up in Bragg geometry with high accuracy is presented. The polychromaticity of the incident wave on the monochromator is accounted for by using a distribution of incoherent point sources along the surface of the crystal. The resulting diffracted amplitude is modified by the sample and can be well represented by a scalar representation of the optical field where the limitations of the usual ‘weak object’ approximation are removed. The subsequent diffraction mechanism on the analyzer is described by the convolution of the incoming wave with the Green-Riemann function of the analyzer. The free space propagation up to the detector position is well reproduced by a classical Fresnel-Kirchhoff integral. The preliminary results of this innovative approach show an excellent agreement with experimental data.

©2007 Optical Society of America

**OCIS codes:** (340.6720) Synchrotron radiation; (340.7440) X-ray imaging; (080.2720) Geometrical optics, mathematical methods; (110.7440) X-ray imaging;

---

## References and links

1. J. Keyriläinen, M. Fernández, S. Fiedler, A. Bravin, M. L. Karjalainen-Lindsberg, P. Virkkunen, E. M. Elo, M. Tenhunen, P. Suortti, and W. Thomlinson, “Visualisation of calcifications and thin collagen strands in human breast tumour specimens by the diffraction-enhanced imaging technique: a comparison with conventional mammography and histology,” *Eur. J. Radiol.* **53** (2), 226 (2005).
2. F. Arfelli, V. Bonvicini, A. Bravin, G. Cantatore, E. Castelli, L. Dalla Palma, M. Di Michiel, M. Fabrizioli, R. Longo, R. -H. Menk, A. Olivo, S. Pani, D. Pontoni, P. Poropat, M. Prest, A. Rashevsky, M. Ratti, L. Rigon, G. Tromba, A. Vacchi, E. Vallazza, and F. Zanconati, “Mammography with synchrotron radiation: Phase-detection techniques,” *Radiology* **215**, 286 (2000).
3. A. Bravin, “Exploiting the x-ray refraction contrast with an analyser: the state of the art,” *J. Phys. D: Appl. Phys.* **36** (10A), A24 (2003).
4. A. Yoneyama, T. Takeda, Y. Tsuchiya, J. Wu, T. T. Lwin, K. Hyodo, and Y. Hirai, “High-energy phase-contrast X-ray imaging using a two-crystal X-ray interferometer,” *J. Synchrotron Radiat.* **12**, 534 (2005).
5. J. Keyriläinen, M. Fernández, and P. Suortti, “Refraction contrast X-ray imaging,” *Nucl. Instrum. Methods A* **488**, 419 (2002).
6. V. Bushuev, E. A. Beliaevskaya, and V. N. Ingal, “Wave optical description of X-ray phase contrast images of weakly absorbing non crystalline objects,” *Il Nuovo Cimento* **19 D**, 513 (1997).
7. T. J. Davis, T. E. Gureyev, D. Gao, A. W. Stevenson, and S. W. Wilkins, “X-ray image contrast from a simple phase object,” *Phys. Rev. Lett.* **74**, 3173 (1995).
8. T. Gureyev, and S. W. Wilkins, “Regimes of X-ray phase contrast imaging with perfect crystals,” *Il Nuovo Cimento* **19 D**, 545 (1997).
9. Y. I. Nesterets, T. E. Gureyev, D. Paganin, K. M. Pavlov, and S. W. Wilkins, “Quantitative diffraction-enhanced X-ray imaging of weak objects,” *J. Phys. D: Appl. Phys.* **37**, 1262 (2004).
10. D. Paganin, T. E. Gureyev, K. M. Pavlov, R. A. Lewis, and M. Kitchen, “Phase retrieval using coherent imaging systems with linear transfer functions,” *Opt. Commun.* **234**, 87 (2004).
11. Y. I. Nesterets, T. E. Gureyev, K. M. Pavlov, D. Paganin, and S. W. Wilkins, “Combined analyser-based and propagation-based phase-contrast imaging of weak objects,” *Opt. Commun.* **259**, 19 (2006).
12. Y. Epelboin, V. Mocella, and A. Soyer, “Optical characteristics of synchrotron sources and their influence in the simulation of X-ray topographs,” *Philos. T. Roy. Soc. A* **357**, 2731 (1999).
13. V. Mocella, Y. Epelboin, and J. P. Guigay, “X-ray dynamical diffraction: the concept of a locally plane wave,” *Acta Cryst. A* **56**, 308 (2000).

14. Y. I. Nesterets, P. Coan, T. E. Gureyev, A. Bravin, P. Cloetens, and S. W. Wilkins, "On qualitative and quantitative analysis in analyser-based imaging," *Acta Cryst. A*, **62** 296 (2006).
15. Y. I. Nesterets, T. E. Gureyev, and S. W. Wilkins, "Polychromaticity in the combined propagation-based/analyser-based phase-contrast imaging," *J. Phys. D: Appl. Phys.* **38**, 4259 (2005).
16. C. A. M. Carvalho, and Y. Epelboin, "Simulation of X-ray traverse topographs and synchrotron Laue topographs: application of the reciprocity theorem," *Acta Cryst. A* **49**, 467 (1993).
17. V. Mocella, Y. Epelboin, and J. P. Guigay, "X-ray dynamical diffraction: the concept of a locally plane wave," *Acta Cryst. A* **56**, 308 (2000).
18. V. Mocella, J. P. Guigay, Y. Epelboin, J. Haertwig, J. Baruchel, and A. Mazuelas, "Influence of the transverse and longitudinal coherence in the dynamical theory of X-ray diffraction," *J. Phys. D: Appl. Phys.* **32**, A88 (1999).
19. T. Uragami, "Pendellösung fringes of X-rays in Bragg case," *J. Phys. Soc. Jpn* **27**, 147 (1969).
20. A. M. Afanas'ev, and V. G. Kohn, "Dynamical theory of X-ray diffraction in crystals with defects," *Acta Cryst. A* **27**, 421 (1971).
21. S. Takagi, "A dynamical theory of diffraction for a distorted crystal," *J. Phys. Soc. Jpn* **26** (1969).
22. J. P. Guigay, "A simple view of the spherical wave in dynamical theory," *Acta Cryst. A*, **55**, 561 (1999).
23. A. Autier, in *Dynamical theory of X-ray diffraction*, (Oxford Press, 2001) Vol. 11.
24. M. Born and E. Wolf, in *Principles of optics: electromagnetic theory of propagation, interference and diffraction of light*, (Cambridge University Press, 1999).
25. A. Autier and D. Simon, "Application de la théorie dynamique de S. Takagi au contraste d'un défaut plan en topographie par rayons X. I. Faute d'empilement," *Acta Cryst. A* **24**, 517 (1968).
26. P. Coan, E. Pagot, S. Fiedler, P. Cloetens, J. Baruchel, and A. Bravin, "Phase-contrast X-ray imaging combining free space propagation and Bragg diffraction," *J. Synchrotron Radiat.* **12**, 241 (2005).
27. P. Coan, A. Peterzol, S. Fiedler, C. Ponchut, J. C. Labiche, and A. Bravin, "Evaluation of imaging performance of a taper optics CCD 'FReLoN' camera designed for medical imaging," *J. Synchrotron Radiat.* **13**, 260 (2006).

## 1. Introduction

X-ray imaging is used for the visualization of internal structures of objects in a large number of fields such as materials science, condensed matter physics, biology and medicine. In absorption imaging, the contrast is generated by variations of the x-ray absorption coefficient arising from density differences and from changes in the thickness and composition of the specimens. The effectiveness of this technique is drastically decreased when the sample consists of elements with low atomic numbers, for which the differences in the hard x-ray absorption coefficients are tiny.

Besides absorption, an x-ray beam traversing an object probes its refractive properties which can also be used as a source of contrast for displaying the internal structure of the sample. The behavior of x-rays as they travel through an object can be described in terms of the complex refraction index,  $n = 1 - \delta - i\beta$ , where the real part  $\delta$  corresponds to the phase shift due to refraction and the imaginary part  $\beta$  to absorption. These changes, which can originate from purely geometrical effects of the shape of the object or, e.g. from local inhomogeneities, cannot often be visualized via absorption imaging. Different techniques have been developed for detecting phase variations. This investigation is focused on the analyzer-based technique (also called "diffraction enhanced imaging"), which has recently been deployed successfully in medical imaging at synchrotron sources [1, 2].

All analyzer-based techniques in their various experimental implementations record the radiation transmitted through an object with the help of an analyzer crystal. The typical set-up consists of a monochromator crystal, a sample, another crystal (analyzer) placed between the sample and the detector, and the detector itself. Images of the diffracted radiation are detected at different angles of the analyzer close to the Bragg condition of the monochromator. The analyzer may be set up in Bragg (reflection) or in Laue (transmission) geometry. Since the refraction angles are of the order of microradians in the x-ray regime, a submicroradian resolution is accordingly needed for recording the refracted x-rays. Owing to that, high stability equipment and crystals with a large degree of perfection are experimentally required for visualizing the refraction contrast [3].

The analyzer in this study is set in Bragg geometry (Fig. 1) and plays a key role in the creation of interference images converting changes of the wave phase into amplitude changes

of the wave field in the analyzer itself and beyond it. This fact and the change of the analyzer's angular position within the limits of its reflectivity curve are sufficient to change the image contrast and for appreciable object details to be viewed. The degree of contrast generated by a refracting object depends on the relative intensities of the waves, corresponding to the object and its background, which pass through the analyzer. Changing the orientation of the analyzer alters these proportions and thereby the contrast. The use of separately mounted crystals allows the limitation in the object size to be overcome, which is characteristic of interferometric techniques [4]. Until now experimental results have been either interpreted in terms of geometrical optics [5] or using wave-optical approaches under a certain number of limiting assumptions. It is clear that the geometrical optics description fails in various circumstances, in particular where the wave nature of the beam cannot be neglected. This is for instance the case in the vicinity of the borders of the object or when the details to be visualized are of the same order of magnitude as the FWHM of the point spread function of the analyzer. In terms of geometrical optics, the phase gradient of a wave passing through an object and taken along the wave front is equal to the local change of the direction of the X-ray propagation. In the case of highly coherent beams, it is possible to generate phase contrast images of small objects at sufficiently large distances after a simple propagation of the wave front even without using an analyzer. Wave-optical approaches are reported in Refs. [6-8], or more recently in Refs. [9-11]. In Ref. [6] a monochromatic plane wave is assumed, and theory is presented assuming the weak-object approximation. Results of their simulations encompassing an analyzer in Laue geometry are in fairly good agreement with experimental data. By working in the Fourier space, Ref. [7] used a more general approach to describe the image contrast from a simple phase object, always using a monochromatic plane wave as a primary source. Deviations of calculated patterns from experimental findings may originate from the plane-wave approximation, as shown by Refs. [12] and [13]. Similar assumptions are also reported in Ref. [8]. The weak-object approximation is introduced also in Refs. [9,10] and [14] to find solutions of the inverse problem (phase and amplitude retrieval) under some assumptions on the object composition. The effects related to the beam polychromaticity have been considered for the first time in Ref. [15] assuming partial coherence and applying the weak-object approximation constraint.

We propose a method which allows computation of the signal generated by an analyzer set-up in Bragg geometry, using as a source a polychromatic spherical wave, with no assumptions on the nature of the object. It also takes into account the combination of the analyzer-based and propagation-based phase contrast which occurs when a coherent beam is used and large distances are there between sample and detector. Numerical results are compared with experimental data and the results of a purely geometrical approach.

## 2. Experimental

The experimental set-up used for our experiments was mounted on the ID19 beamline at the ESRF, and includes a pre-monochromator (fixed-exit double crystal Si(111) in Laue geometry) reducing the incoming continuous energy spectrum to an energy resolution  $\Delta E/E = \Delta\lambda/\lambda \cong 5 \times 10^{-4}$  ( $\lambda = 0.496 \text{ \AA}$ ), a symmetrically cut, 3 cm thick Si(111) Bragg monochromator and an identical analyzer (non dispersive setting) as shown in Fig.1.

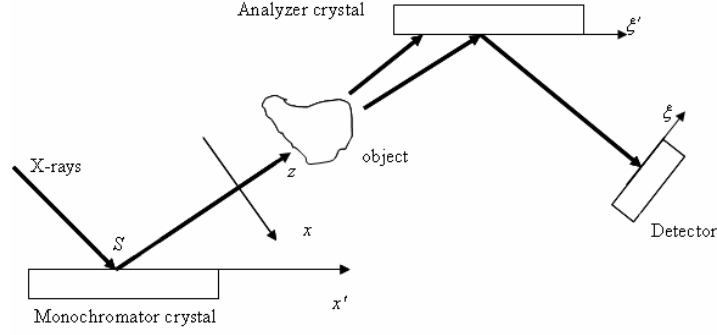


Fig. 1. Schematic layout of the experimental set-up for analyzer-based imaging with synchrotron radiation. The premonochromator is not shown.  $x$ ,  $x'$ ,  $\xi$  and  $\xi'$ : coordinate directions (see text).

The incident radiation on the Bragg monochromator is a polychromatic  $\sigma$ -polarized beam. The polychromaticity is accounted for in a straightforward way by using a distribution of incoherent point sources along the surface of the crystal, as it was shown in Refs. [12] and [16-17]. It should be underlined that this is not an approximation: when the polychromaticity of the incident beam is much larger than the wavelength acceptance of the diffracting crystal, which is typically the case at synchrotron facilities, the illumination on the entrance surface is completely incoherent. For the simulation it is assumed that both crystals, monochromator and analyzer, are perfect. The incoherence assumption implies that calculations can be performed independently for each point source along the surface of the monochromator (absorption is also taken into account).

### 3. Theory

In our set-up the longitudinal coherence length along the propagation direction is  $\lambda^2 / \Delta\lambda = 0.1 \mu\text{m}$ . The projection along the crystal surface would imply an additional factor ( $\cos(\theta_{\text{Bragg}}) = \cos(4.5^\circ)$ ) which is very close to 1. As a consequence, partial coherence should be considered only for distances between points along the crystal surface smaller than  $0.1 \mu\text{m}$ , which is the minimum calculation step used here. The incoherence assumption is thus fully justified [18].

The amplitude diffracted from the monochromator is given by the Kato spherical wave solution, as derived from dynamical diffraction theory [19,20], which corresponds to the Green-Riemann function of the Takagi-Taupin (T-T) equations for perfect crystals [21,22].

In the present case the expression of the diffracted Kato spherical wave as a function of the  $x'$  coordinate along the entrance surface is [23]:

$$R_h(x', S) = -i\pi Ck\chi_h \left[ J_0 \left( (x' - S) \frac{\pi k C}{\sin \theta_B} \sqrt{\chi_{\bar{h}} \chi_h} \right) + J_2 \left( (x' - S) \frac{\pi k C}{\sin \theta_B} \sqrt{\chi_{\bar{h}} \chi_h} \right) \right] \quad (1)$$

where  $\chi_{\bar{h}}$  and  $\chi_h$  are the Fourier components of the dielectric susceptibility associated with the reciprocal lattice vector  $\mathbf{h}$ ,  $C$  is the polarization factor ( $=1$  for  $\sigma$ -polarization),  $k=1/\lambda$  ( $\lambda$  is the x-ray wavelength and  $J_0$  and  $J_2$  are the zero-th and second order Bessel function, respectively. The point  $S$  referred to in (1) is shown in Fig. 1. Indicating the deviation from unity of the complex refractive index  $n$  of the object as:

$$1 - n(x, z) = \delta(x, z) + i\beta(x, z) \quad (2)$$

the complex phase modulation introduced by the object is:

$$\Phi(x) = \frac{2\pi}{\lambda} \int (\delta(x, z) + i\beta(x, z)) dz \quad (3)$$

Its transmission function  $A(x)$  can be expressed as:

$$A(x) = e^{i\Phi(x)} = A_0(x) e^{i\varphi(x)} \quad (4)$$

where  $A_0(x)$  describes the absorption and  $\varphi(x)$  the associated real phase modulation. Using (3) we can write:

$$A_0(x) = e^{-\frac{2\pi}{\lambda} \int \beta(x,z) dz} \quad (5)$$

$$\varphi(x) = \frac{2\pi}{\lambda} \int \delta(x,z) dz \quad (6)$$

The integral in (4) is computed numerically without resorting to the usual weak-object approximation:  $e^{i\varphi(x)} \approx 1 + i\varphi(x)$ , which is not needed for our simulation purposes. In a scalar representation of the optical field [24] the spherical wave emitted by the first crystal is modified by the transmission function of the object. Downstream from the latter, the wave complex amplitude along the transverse direction  $x$  is given by:

$$\psi(x, S) = R_h(x, S) A(x) \quad (7)$$

This is the incident wave on the analyzer. The diffraction mechanism of this wave on the analyzer is described by its convolution with Eq. 1 [21,25]:

$$\Upsilon(\xi', S) = \int \psi(\tau, S) R_h(\xi' - \tau, S) d\tau \quad (8)$$

where  $\xi'$  is the coordinate along the analyzer surface (Fig. 1).

In paraxial approximation, the free space propagation after the analyzer is described by a Fresnel-Kirchhoff convolution integral. In particular, the amplitude at the detector position due to an individual point source  $S$  along the monochromator is given by:

$$\Psi(\xi, S) = \int \Upsilon(\tau, S) e^{-\frac{i\pi k(\xi - \tau)^2}{L}} d\tau \quad (9)$$

where  $\xi$  is the coordinate along the detector surface. In (9) terms not essential for the calculation of the intensity have been omitted.

Making use of the commutative properties of convolution integrals, it is easy to verify in Fourier space that the only relevant distance is the total distance  $L$  between object and detector. Finally, the total intensity recorded by the detector is the incoherent sum over  $S$  of individual point-source contributions:

$$I(\xi) = \int |\Psi(\xi, S)|^2 dS \quad (10)$$

#### 4. Comparisons with experimental results and conclusion

Equations (1)-(10) have been used in the numerical simulation of the set-up in Fig. 1. The results are shown in Figs. 2 to 5, where experimental results and theoretical predictions of the intensity patterns by both the geometrical [5] and the current wave-optical approach are compared.

For the experimental results reported in Fig. 2 and Fig. 3, the detector used was a CCD camera (pixel size  $7 \times 7 \mu\text{m}^2$ ), the x-ray energy 25 keV, the samples two cylindrical fibers, one of Kevlar and one of nylon with radii  $50 \mu\text{m}$  and  $175 \mu\text{m}$ , respectively; two values of the sample-to-detector-distance  $L$  were chosen, i.e. 0.5 and 5.5 m. The angular offset  $\theta_a$  of the analyzer was also varied during the measurements, and data are showed for  $\theta_a=0$  and  $\theta_a=-11.7$   $\mu\text{rad}$ . The point-spread function of the detector with a FWHM of  $10 \mu\text{m}$  has been taken into

account. It should be noted that the agreement of either approach with the experimental data is good for  $L=0.5$  m but the geometrical model fails at  $L = 5.5$  m.

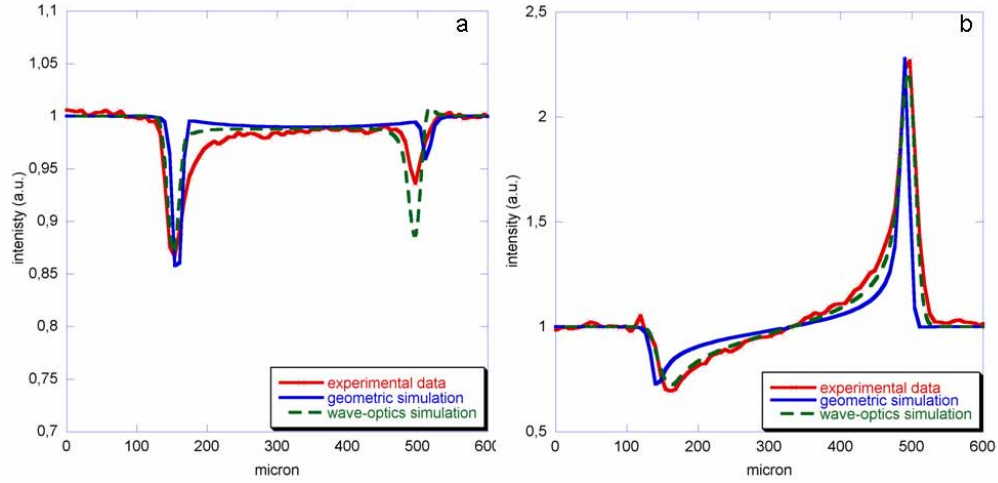


Fig. 2. (a). Intensity pattern (a. u.): experimental (red), geometrical (blue) wave-optical (dashed green): Si(111) reflection,  $\theta_a = 0$   $\mu$ rad, nylon,  $R = 175$   $\mu$ m,  $L = 0.5$  m; (b) Intensity pattern (a.u.); experimental (red), geometrical (blue) wave-optical (dashed green): Si(111) reflection,  $\theta_a = -11.7$   $\mu$ rad, nylon,  $R = 175$   $\mu$ m,  $L = 0.5$  m.

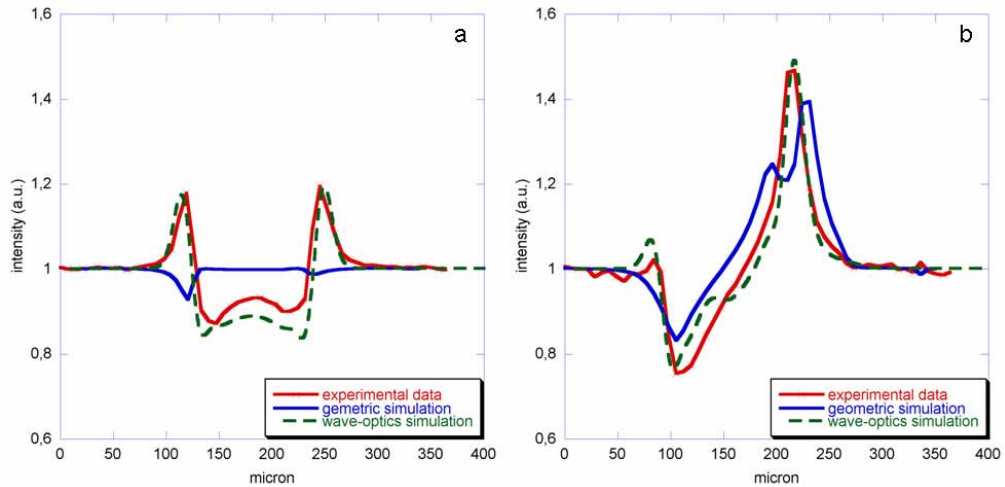


Fig. 3. (a). Intensity pattern (a.u.); experimental (red), geometrical (blue) wave-optical (dashed green): Si(111) reflection,  $\theta_a = 0$   $\mu$ rad, Kevlar,  $R = 50$   $\mu$ m,  $L = 5.5$  m; (b) Intensity pattern (a.u.); experimental (red), geometrical (blue) wave-optical (dashed green): Si(111) reflection,  $\theta_a = -11.7$   $\mu$ rad, Kevlar,  $R = 50$   $\mu$ m,  $L = 5.5$  m.

This is not surprising because when free-space propagation occurs over larger distances, interference effects, which can be taken into account only by the wave-optical model, play an essential role [11, 26]. The slight differences (smaller than 5%) between experiment and wave-optical theory, noticeable especially in the case of  $\theta_a=0$  for both fibers, are possibly due to the simplifying assumption that the crystals are perfect. Considering the (slightly broader) experimental reflectivity profile instead would not help improve the accuracy of the simulation, since in this case the information about the associated phase is missing. The

asymmetry of both the experimental and the theoretical peaks for  $\theta_a=0$  is a signature of the slight asymmetry of the crystal reflectivity curves with respect to their exact Bragg positions. The amount of asymmetry is strongly dependent on the shape of the resulting transfer function of the monochromator-analyzer subsystem, the angular change being of opposite sign on the two sides of the curve. In particular, this change is weighted by the curve flank slopes which appear to be the steepest when the two crystals are perfectly aligned. The slope variations of the monochromator-analyzer transfer function are less dramatic for  $\theta_a \neq 0$ , as it was shown by [15]. This fact is reflected in the smoother behavior of the corresponding intensity profiles [Figs 2(b) and 3(b)], though the intensities are higher since the contrast in the image strongly depends on the deviation of the analyzer from the exact Bragg position.

Two more samples were imaged using a taper optics CCD camera (pixel size  $47 \times 47 \mu\text{m}^2$ ) [27] placed at 2.2 m from them and at an X-ray energy of 51.5 keV. The first sample is a triangular plexiglas wedge [see Fig. 4(a)], while the second one is a trapezoidal wedge of the same material and is depicted in Fig 4(b). The angle  $\theta_a$  was also varied during the measurements. The data shown in Fig. 5(a) and Fig. 5(b) refer to  $\theta_a=3.4 \mu\text{rad}$  and  $\theta_a=-3.4 \mu\text{rad}$ , respectively.

Differently from the previous ones, these samples are large and thick. The agreement between the simulations and the experimental data is as good as 99 %. This highlights the added value of the presented approach and substantiates its capability to cope with sizeable samples far away from the limit imposed by the usual weak object approximation.

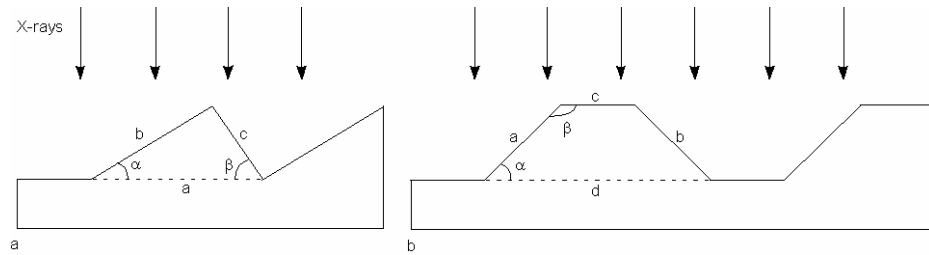


Fig. 4. (a). Triangular plexiglas wedge;  $a=3 \text{ mm}$ ,  $b=2.6 \text{ mm}$ ,  $c=1.5 \text{ mm}$ ,  $\alpha=30^\circ$ ,  $\beta=60^\circ$ ; (b) Trapezoidal plexiglas wedge;  $a=b=1.5 \text{ mm}$ ,  $c=2 \text{ mm}$ ,  $d=4.12 \text{ mm}$ ,  $\alpha=45^\circ$ ,  $\beta=135^\circ$ . The arrows indicate the incident X-ray beam direction.

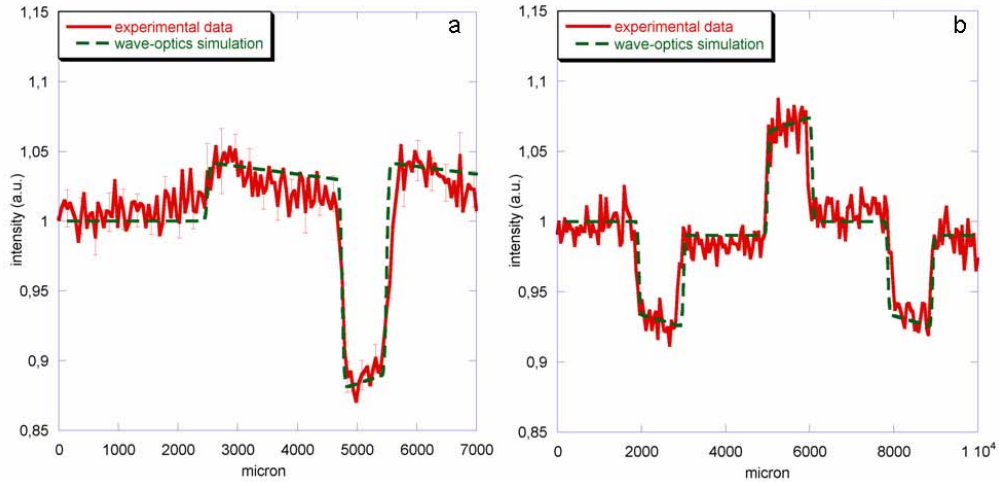


Fig. 5. (a). Intensity pattern (a.u.): experimental (red) and wave-optical (dashed green) for the triangular wedge as in Fig. 4(a), Si(111) reflection,  $\theta_a = 3.404 \mu\text{rad}$ ,  $L=2.2 \text{ m}$ ; (b) Intensity pattern (a.u.): experimental (red) and wave-optical (dashed green) for the trapezoidal wedge as in Fig. 4(b), Si(111) reflection,  $\theta_a = -3.404 \mu\text{rad}$ ,  $L=2.2 \text{ m}$ .

Summarizing, the excellent agreement between simulation and data gives a high level of confidence in the presented wave-optical approach, which will be used prospectively for other samples with more complex shapes and for higher order reflections. More importantly, it is foreseen to include the modeling of crystal systems in dispersive configurations. Once validated entirely, this method might be routinely integrated into parametric studies for optical design optimization of analyzer-based phase contrast imaging set-ups.

### Acknowledgments

We gratefully acknowledge the help of Mr. Greg Johnson for helping in compiling the Matlab simulation code on the ESRF central computing facility.